JOURNAL OF GEOPHYSICAL RESEARCH, VOL. 102, A5, DOI:10.1029/96JA03826, MAY 1997

Upstream whistlers generated by protons reflected from a quasi-perpendicular shock

P. Hellinger

Institute of Atmospheric Physics, Prague, Czech Republic

A. Mangeney

Observatory of Paris, Meudon, France

Abstract. Numerical simulations of collisionless supercritical quasi-perpendicular shocks suggest that the upstream whistlers may be generated near the shock by the reflected protons which gyrate back to the shock. We investigate in detail results of hybrid simulations and a linear theory for a gyrotropic gyrating beam in a Maxwellian plasma, and we compare their outcomes. We find good agreement between the linear theory and the simulations. We compare these theoretical issues with observations, and we discuss the results. We also discuss dimensionality effects on the simulations of upstream whistlers. The investigation of lower Mach shocks leads us to a condition for the existence of a so-called shock rippling.

1. Introduction

Upstream whistlers are often found upstream of collisionless shocks in interplanetary space. They were first observed by *Russell et al.* [1971] using data obtained from OGO 5 in the upstream region of the Earth's bow shock. A detailed study by *Fairfield* [1974] indicated that the waves observed in this region and in the frequency range 0.5-4 Hz are whistler modes propagating in an extended region upstream of the shock, obliquely with respect to the ambient magnetic field. Later on, similar waves were discovered upstream of other planetary shocks [*Orlowski et al.*, 1990, 1992; *Orlowski and Russell*, 1991], and it was proposed by *Orlowski et al.* [1994] to call them upstream whistlers to distinguish them from the "foot whistlers," found in the immediate vicinity of the shock ramp.

The generation mechanism and source location of these upstream whistlers have not yet been clearly identified. Broadly speaking, two possible scenarios have been proposed: the first one is a generation by and within the shock itself, the second one is a local generation upstream by particles reflected from the shock. The first scenario was proposed by *Fairfield* [1974], who did not suggest a definite generation mechanism. An objection was raised against such a scenario: since the waves can be observed far upstream of the shock, they should be weakly damped during their propagation from the source to the observer; however, studies by *Rodriguez and Gurnett* [1975] and *Greenstadt et al.* [1981] suggested that shock-generated whistlers were heavily damped in the foot of the shock.

A theory for the local generation of whistler waves by anisotropic or gyrophase-bunched beams of protons was developed by *Wong and Goldstein* [1987, 1988]. However, the waves are observed [*Hoppe et al.*, 1982] even when such beams are not recorded.

Nonthermal electrons were also invoked by *Sentman et al.* [1983] because upstream whistlers are observed when suprathermal electrons with large pitch angle [*Feldman et al.*, 1983] are detected. However, a recent study by *Orlowski et al.* [1995] indicates that upstream of the Earth's bow shock the observed electron distribution function is stable against the generation of whistler waves; therefore the waves should be damped in the upstream region in agreement with the observations by *Orlowski and Russell* [1991], who showed that the amplitudes decreased with increasing distance from the shock.

0148-0227/04/96JA03826$9.00

Orlowski et al. [1995] also pointed out that the damping scale length of whistler waves can vary by an order of magnitude with small changes in the form of the electron velocity distribution function so that the hypothesis of generation of upstream whistlers in the shock layer can be reconciled with the fact that they are, at times, observed far upstream.

Therefore the hypothesis that upstream whistlers are generated in the vicinity of the shock ramp, suggested by the above mentioned observations is again considered as a viable one.

What precisely is this generating mechanism? A variety of cross-field drift or anisotropy-driven instabilities may arise within the shock ramp. The favored ones are related to the electron dynamics in the shock ramp which is still poorly understood. For example, loss cone distributions or nongyrotropic distributions may become unstable for oblique whistler waves [*Veltri and Zimbardo*, 1993]. Electron beams may be also responsible for the generation of oblique whistler waves [*Tokar and Gurnett*, 1985] within the shock ramp.

On the other hand, the proton dynamics are now very well understood. The shock is able to reflect up to about $20-30\%$ of incident protons. The analysis of the results of numerical simulations led *Krauss-Varban et al.* [1995] and *Hellinger et al.* [1996] to propose that the oblique whistlers may be generated by these gyrophase-bunched reflected protons. The mechanism is the same as proposed for the local upstream generation by *Wong and Goldstein* [1988], except the whistlers are generated by the reflected protons gyrating back toward the shock.

In this paper we want to extend the work by *Hellinger et al.* [1996] (referred to as paper 1) and *Wong and Goldstein* [1988] and to give a more quantitative comparison between the results of the numerical simulations and the linear theory. In paper 1 we have also mentioned that no Alfvén ion cyclotron (AIC) waves were observed in slightly supercritical quasi-perpendicular shocks; we shall revisit this problem and give a simple explanation for the absence of AIC waves in these shocks.

Finally, we shall discuss the differences between numerical simulations in two and three space dimensions and compare our results with those obtained by *Krauss-Varban et al.* [1995].

2. Simulations

2.1. Code

Our simulations were made using a three-dimensional (3-D) version of a hybrid code written by *Matthews* [1994]. This code only uses one computational pass through the particle data and allows a field time substepping. These features make the code convenient for 3-D simulations.

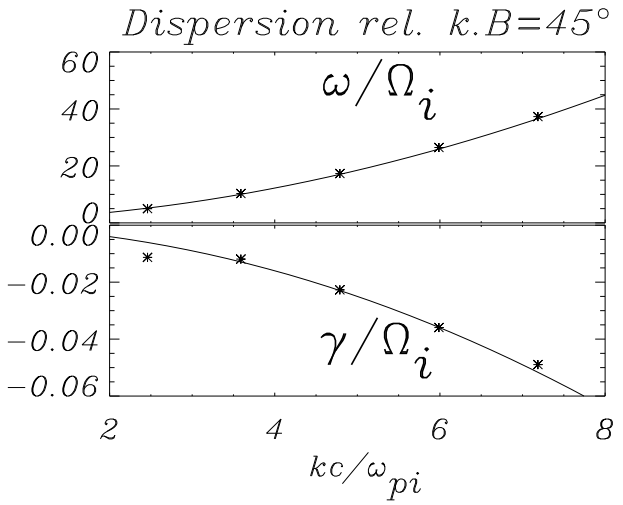

Figure 1. Dispersion relations (top) $\omega(k)$ and (bottom) $\gamma(k)$ (bottom panel) for the whistler mode with $\theta_{kB} = 45\,\mathrm{deg}$. Results of the linear theory are denoted by solid curves, results of the simulation are denoted by asterisks.

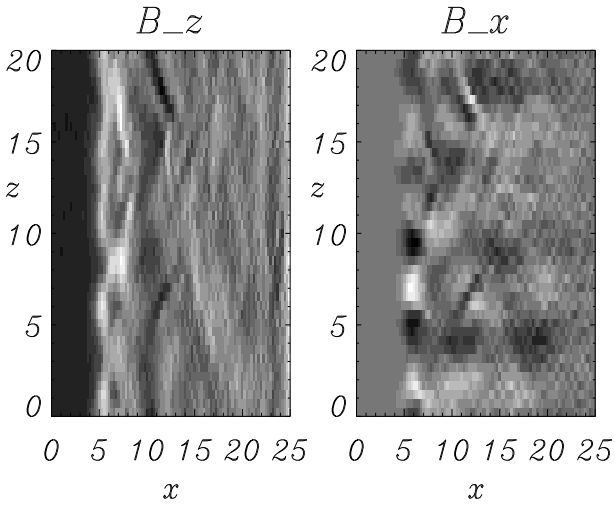

Figure 2. Two dimensional (2-D) grey level plots (left) of the compressional component B_z and (right) of the transverse component B_x in the coplanarity plane for the shock with $M_A = 5$. Distances are in units of c/ω_{pi}.

Units of space and time are c/ω_{pi} and Ω_i, respectively, where c is the speed of light, $\omega_{pi} = \{n_0 e^2/m_p\epsilon_0\}^{1/2}$ is the upstream proton plasma frequency, and $\Omega_i = eB_0/m_p$ is the upstream proton gyrofrequency (n_0 and B_0 are the upstream density and magnitude of the magnetic field, respectively, while e and m_p are the proton electric charge and mass, respectively; finally, ϵ_0 and μ_0 are the dielectric and magnetic permeabilities of vacuum), respectively. The spatial resolution is $dx = dz = 0.125c/\omega_{pi}$ and $dy = 0.25c/\omega_{pi}$. There are 15 particles per cell in the region upstream of the shock; fields and moments are defined on a 3-D grid with dimensions $n_x \times n_y \times n_z = 200 \times 20 \times 40$, where x is the coordinate along the shock normal direction. The time step for the particle advance is $dt = 0.05\Omega_i^{-1}$, while the magnetic field **B** is advanced with a smaller time step $dt_B = dt/20$.

The shock is launched in the standard way by reflection of a streaming plasma on an infinitely conducting wall located at $x = 25$. The parameters of the simulation are plasma injection velocity, $v_0 = 2v_A$, directed parallel to the x axis, angle between the shock normal and the upstream magnetic field vector (in the coplanarity plane xz), $\theta_{Bn} = 80^o$, the proton and electron pressures normalized to the upstream magnetic pressure, $\beta_p = \beta_e = 0.5$, and resistivity, $\eta = 10^{-3}\mu_0 v_A^2/\Omega_i$ ($v_A = B_0/\sqrt{\mu_0 n_0 m_p}$ is the upstream Alfvén speed).

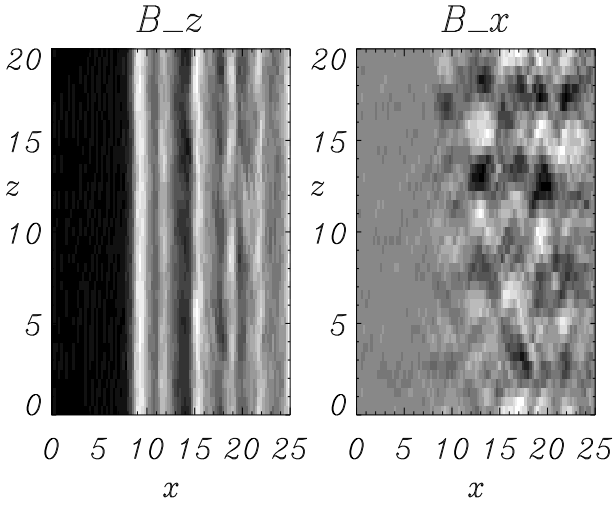

Figure 3. The 2-D grey level plots (left) of the compressional magnetic component B_z and (right) of the transverse component B_x in the coplanarity plane for the shock with $M_A = 3.3$. Distances are in units of c/ω_{pi}.

2.2. Tests at High Frequencies

Since we want to study the generation of relatively high-frequency whistler waves (about $20 - 40\Omega_i$), we have to make sure that the code gives results which are physically meaningful in this high-frequency region.

We have therefore considered the propagation of small amplitude whistler waves in a Maxwellian plasma using a one-dimensional (1-D) version of the code and compared with the predictions of the linear theory [using the program WHAMP by *Rönmark*, 1982].

Two points should be mentioned. First, the theoretical dispersion relation was calculated for the same β_p as in the simulations but with a small value of $\beta_e = 0.003$ in order to suppress the electron kinetics.

The second point is that the damping rate due to the protons is of the order $10^{-4}\Omega_i$ and is negligible with respect to the resistive damping rate γ_{res} given by

$$\gamma_{\mathrm{res}} \simeq \frac{\eta}{\mu_0} k^2 \qquad (1)$$

for the value of the resistivity η used here. We have therefore compared the damping rate obtained in the simulation with the resistive one (equation (1)). A typical example of the results of the comparison is shown on Figure 1. On Figure 1 we have plotted the frequency ω and damping rate γ obtained from the 1-D simulations (asterisks) and the linear theory (solid curves) for oblique propagation, $\theta_{kB} = 45\,\mathrm{deg}$ (θ_{kB} is the angle between the wave vector **k** and the magnetic field **B**). One may see that even for the high frequencies $\sim 30\Omega_i$ there is a very good agreement between the simulation results and the linear theory. Thus we may conclude that the code can be used safely to describe timescales as short as $(20 - 40\Omega_i)^{-1}$ as long as it is justified to ignore electron kinetic effects.

2.3. Results

With the parameters we used, we have observed the formation of a slightly supercritical quasi-perpendicular shock with an Alfvén Mach number $M_A \simeq 3.3$ traveling in the direction of decreasing

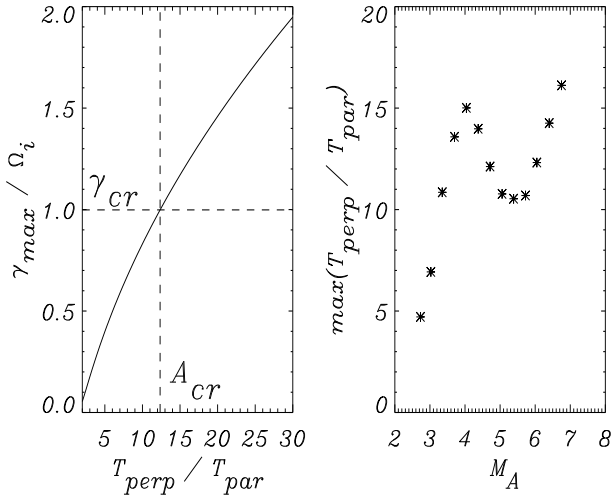

Figure 4. (left) The results of the linear theory, the dependence of the maximum growth rate of the Alfvén ion cyclotron waves on the proton temperature anisotropy. The horizontal dashed line denotes $\gamma_{cr} = \Omega_{il}$, the vertical dashed line denotes the corresponding $A_{cr} \simeq 12.5$. (right) The results of the 2D shock simulations, the maximum of the shock temperature anisotropy as a function of the Alfvén Mach number (asterisks).

x. Its overall properties are what one could expect in this regime and are described in paper 1. We want to focus here on two particular points: the absence of Alfvén ion cyclotron (AIC) waves in the shock ramp and the excitation of upstream whistlers.

2.3.1. Alfvén ion cyclotron waves

The Alfvén ion cyclotron (AIC) waves play an important role in the relaxation of ion temperature anisotropies associated with the quasi-perpendicular shocks [*Gary et al.*, 1993]. The two-dimensional (2-D) simulations show that in high Mach number quasi-perpendicular shocks, AIC instability is active and causes a significant "rippling" of the shock front [*Winske and Quest*, 1988; *Thomas and Brecht*, 1986; *McKean et al.*, 1995]. The AIC instability results from the large effective temperature anisotropy due to the presence of reflected protons in the shock front [*Burgess*, 1987; *Skopke et al.*, 1983]. The excited waves have compressional magnetic and density fluctuations of the same order of magnitude as that of the transverse ones, and their wave vector is parallel or slightly oblique to the shock front with a wavelength of $3-5c/\omega_{pi}$, similar to but lower than those found in the linear theory of the AIC instability in an homogeneous plasma [*Winske and Quest*, 1988].

Thomas and Brecht [1986] have studied the properties of quasi-perpendicular shocks in a broad range of parameters, using a 2-D hybrid code; in their results it can be seen that AIC waves are excited in the shock ramp with a significant amplitude only when the Mach number is large enough.

For example, their case I, a shock with $M_A = 3.5$ ($\beta_p = \beta_e = 0.5$), clearly shows no compressional fluctuations along the shock front contrary to the case of higher Mach number shocks. The transverse (to the shock normal) fluctuations appear only downstream behind the shock front.

We have obtained similar results. For example, Figures 2 and 3 illustrate the results of 2-D simulations for two supercritical shocks with $M_A = 5$ and $M_A = 3.3$, respectively, (other parameters are identical: $\theta_{nB} = 80\,\mathrm{deg}$, $\beta_e = \beta_p = 0.5$ upstream, and $dx = dz = 0.5c/\omega_{pi}$; the dimensions of the simulation box are $25c/\omega_{pi} \times 20c/\omega_{pi}$; the simulation box is chosen to lie in the coplanarity plane; and the results are shown at the time $t = 12\Omega_i^{-1}$).

In Figures 2 and 3 we present 2-D grey level plots of the compressional magnetic component B_z and a similar plot for one transverse component B_x. The shock ramp is clearly rippled in the first case and not rippled in the second. In this case, one can see the development of standard AIC waves behind the shock front which are transported with the flow farther downstream: the shock front is clearly unaffected by their presence.

This difference between the low and high Mach number quasi-perpendicular shocks may be explained in the following way. The region where high-temperature anisotropies can be found is bounded by the shock front on one side and the end of the shock foot at the other side. Its thickness is typically $d \sim 0.3v_0/\Omega_i$ [*Gedalin*, 1996], if v_0 is the upstream bulk velocity in the shock frame. So the growth time $t_\gamma = 1/\gamma$ (γ is the growth rate of the instability) of a wave should be shorter than the time $t_c = d/v_c$ needed by the plasma to cross the unstable region with a velocity which may be estimated as $v_c \sim (v_0 + v_1)/2$, where v_1 is the downstream plasma bulk velocity in the shock frame (we neglect the phase velocity of the mode). Using the Rankine-Hugoniot relation $n_0 v_0 = n_1 v_1$, where n_1 is the downstream density, we find a condition for the existence of AIC rippling of the shock front:

$$\gamma > \gamma_{cr} \simeq 1.6(1 + \frac{n_0}{n_1})\Omega_i > \Omega_{il} \qquad (2)$$

where Ω_{il} and Ω_{id} are respectively the local and downstream gyrofrequencies, respectively,

$$\Omega_{il} \sim 0.5(\Omega_i + \Omega_{id}) \sim 2\Omega_i$$

Homogeneous linear theory predicts that there exist unstable AIC waves with $\gamma > \Omega_{il}$ in a bi-Maxwellian plasma with $A = T_\perp/T_{||} > 12$ (for $\beta_{p||} = 0.5$). The comparison of this simple theoretical condition and 2-D shock hybrid simulations is shown on Figure 4. Figure 4 (left) shows how the maximum AIC growth rate $\gamma_{\max}$ depends on the (proton) temperature anisotropy ratio $T_\perp/T_{||}$. The horizontal dashed line denotes the critical growth rate $\gamma_{cr} = \Omega_{il}$ and the vertical dashed line denotes the corresponding $A_{cr} \simeq 12.5$. On the right is the maximum, along the shock normal, of the temperature anisotropy measured in 2-D simulations as a function of the Mach number (the temperatures were averaged over planes parallel to shock front before computing the anisotropy ratio).

It can be seen that low Mach number quasi-perpendicular shocks have their maximum temperature anisotropy lower than the threshold $A^*_{cr} \sim 15$ and that the transition toward unstable AIC waves takes place around $M_A^{\mathrm{AIC}} \sim 4$, as observed in the numerical simulations. The critical maximum anisotropy A^*_{cr} found in the simulation is in good agreement with the critical anisotropy A_{cr} predicted by the linear theory; the small difference is probably due to the uncertainties in the estimates of the plasma parameters in the shock front region.

Note that in the interval $M_A \sim 4-5$ the temperature anisotropy ratio decreases, an effect which is simply related to the development of AIC ripples on the shock front. Indeed, the region of high anisotropy is also rippled, and an average along planes perpendicular to the overall shock normal mixes regions of low and high anisotropy, resulting in a lower temperature anisotropy.

We have shown that below some critical Mach number M_A^{AIC} there is no important AIC wave activity in the shock front. The supercritical quasi-perpendicular shock waves with Mach numbers below M_A^{AIC} are an intermediate case between the highly supercritical [*McKean et al.*, 1995] and subcritical [*McKean et al.*, 1996] shocks.

In the 3-D simulation which we shall discuss below, where $M_A \simeq 3.3 < M_A^{\mathrm{AIC}}$, no significant level of AIC waves in the shock front is to be expected in agreement with the simulation results.

2.3.2. Upstream whistlers

As discussed in paper 1, we see a right-handed mode which appears to belong to the whistler branch of the fast magnetosonic mode. This mode is generated somewhere near the shock and propagates upstream, obliquely both to the magnetic field and to the shock normal (the angle between the wave vector and the mean magnetic field is $\theta_{kB} \simeq 131\,\mathrm{deg}$, between the wave vector and the shock normal is $\theta_{kn} \simeq 51\,\mathrm{deg}$, and between the wave vector and the coplanarity plane is $\theta_{kc} \simeq 56\,\mathrm{deg}$). Its wavelength is $\lambda \simeq c/\omega_{pi}$, and its frequency is $\omega \simeq 27\Omega_i$.

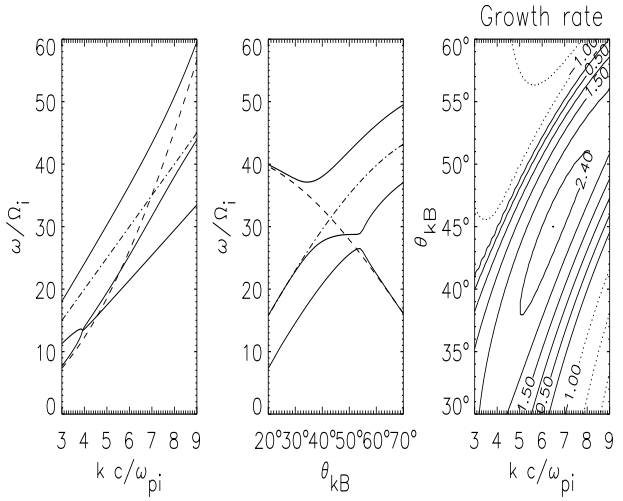

Figure 5. (left) and (middle) The dispersion properties $\omega(k, \theta_{kB})$ of the three branches (solid curves) in the gyrating beam - plasma system. The value ω as function of k for $\theta_{kB} = 45\,\mathrm{deg}$ is shown (left) and the ω as function of θ_{kB} for $k = 7\omega_{pi}/c$ is shown (middle). For comparison, we plot also the Maxwellian whistlers dispersion relation (dashed curve) and the resonance condition $\omega = \mathbf{k} \cdot \mathbf{v}_b$ (dot-dashed curve). (right) The 2-D contour plot of the growth rate $\gamma(k, \theta_{kB})$ for the intermediate branch (note that the negative values of γ are dotted).

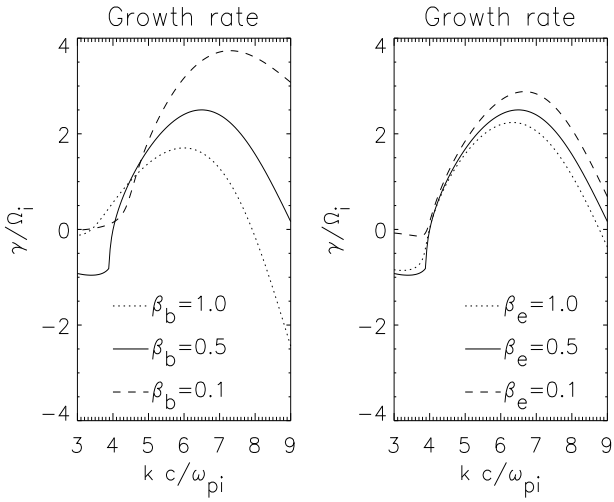

Figure 6. (left) The growth rate as function of k for $\theta_{kB} = 45\,\mathrm{deg}$ for three different values of β_b: $\beta_b = 1.0$ (dotted curve), $\beta_b = 0.5$ (solid curve), and $\beta_b = 0.1$ (dashed curve). (right) The growth rate as function of k for $\theta_{kB} = 45\,\mathrm{deg}$ for three different values of β_e: $\beta_e = 1.0$ (dotted curve), $\beta_e = 0.5$ (solid curve), and $\beta_e = 0.1$ (dashed curve).

3. Comparison With a Linear Theory

In paper 1 we suggested that the wave mode observed in the simulation was generated by the reflected protons gyrating back to the shock, on the basis that its properties were comparable to those expected from the linear theory and that it is resonant with the population of reflected particles. In this section we want to compare quantitatively the predictions of the linear theory with the results of 3-D simulations. We shall do the comparison in three steps: In the first part we shall study the general dispersion properties of the beam-plasma system. We shall also regard the influence of the plasma and beam parameters on the instability; this study will be useful for later discussions. In the second part we shall test the prediction of the instability by means of a 1-D hybrid simulation. Finally, in the third part we shall compare the predictions of the linear theory with the results of the 3-D shock simulation. We shall also compare the quasi-linear behavior of the instability in the 1-D and 3-D simulations.

3.1. Properties of the Instability for a Gyrating Beam

The generation of obliquely propagating whistler waves by a proton beam instability in the context of collisionless shock physics has been considered by a number of authors [e.g., *Wong and Goldstein*, 1988, and references therein]. We have adopted the approach of *Wong and Goldstein* [1988] and made a thorough investigation of the stability of a gyrating gyrotropic proton beam with a bi-Maxwellian distribution function

$$f_b = \frac{n_b}{\sqrt{\pi}^3 v_{th\perp b}^2 v_{th||b}} \times \exp\left(-\frac{(v_x - v_{0\perp b})^2}{v_{th\perp b}^2} - \frac{v_y^2}{v_{th\perp b}^2} - \frac{(v_z - v_{0||b})^2}{v_{th||b}^2}\right) \quad (3)$$

drifting with a velocity $\mathbf{v}_{0b} = (v_{0\perp b}, 0, v_{0||b})$ with respect to a Maxwellian plasma in the presence of an unperturbed magnetic field $\mathbf{B}_0 = (0, 0, B_0)$ directed along the z axis.

We have limited ourselves to the high-frequency range $\omega >> \Omega_b$, where the beam gyration may be neglected. We have also assumed charge neutrality $n_e = n_b + n_p$, where n_p, n_e, and n_b are the background proton density, the total electron density, and the proton beam density, respectively. The following parameters have been used (if not explicitly stated otherwise): ratio of the electron plasma frequency to the electron gyrofrequency, $\omega_{pe}/\Omega_e = 200$; ratio of the beam density to the electron density, $n_b/n_e = 0.1$; parallel proton beam temperature $T_{b||} = T_p$ equal to the background proton temperature T_p; and beam velocity, $v_b = 7.07 v_A$, where the Alfvén speed $v_A = B_0/\sqrt{\mu_0 m_p n_e}$ is calculated with the background magnetic field magnitude B_0 and the total electron density n_e. The details of the analysis can be found in the appendix; here we shall only present the main results.

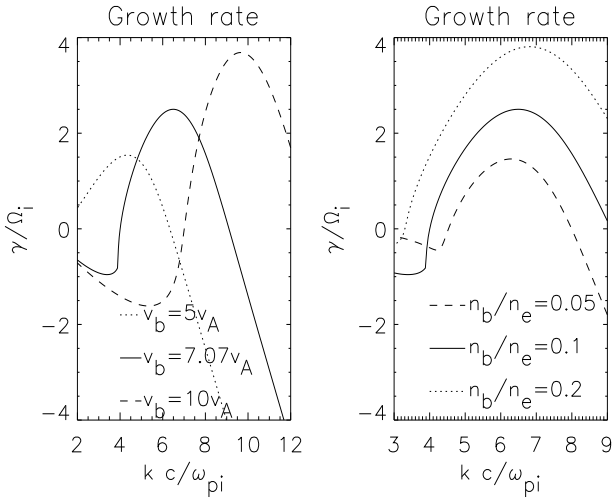

Figure 7. (left) The growth rate as function of k for $\theta_{kB} = 45\,\mathrm{deg}$ for three different values of v_b: $v_b = 5$ (dotted curve), $v_b = 7.07$ (solid curve), and $v_b = 10$ (dashed curve). (right) The growth rate as function of k for $\theta_{kB} = 45\,\mathrm{deg}$ for three different values of n_b/n_e: $n_b/n_e = 0.05$ (dashed curve), $n_b/n_e = 0.1$ (solid curve), and $n_b/n_e = 0.2$ (dotted curve).

With these parameters and when the beam velocity is parallel to the magnetic field, the (real) frequency for a given wave vector and direction of propagation remains close to the value obtained for a purely Maxwellian plasma. However, when the beam veloc-

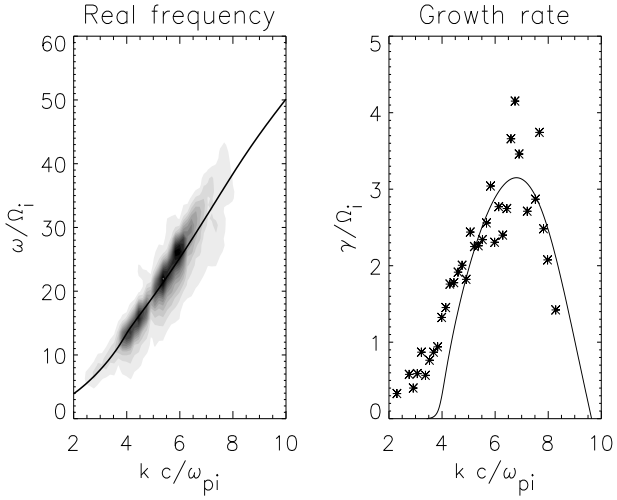

Figure 8. (left) The dispersion relation $\omega(k)$ for $\theta_{kB} = 45\,\mathrm{deg}$: the solid curve denotes the result of the linear theory. The gray level plot shows the result of the real frequency in the simulation. (right) The growth rate $\gamma(k)$ for $\theta_{kB} = 45\,\mathrm{deg}$: the solid curve denotes the result of the linear theory, the asterisks denote the results of the simulation.

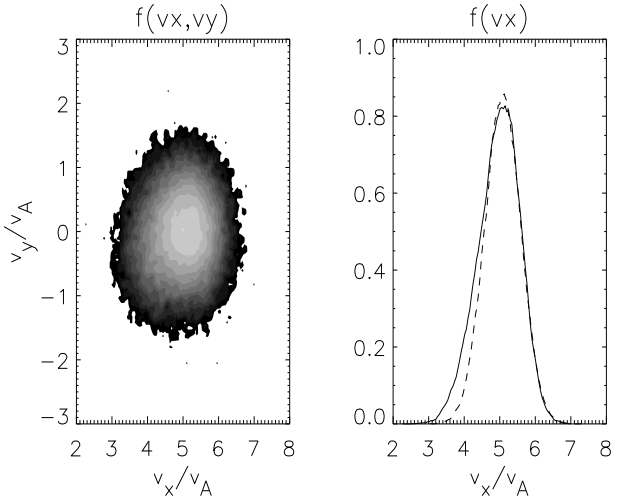

Figure 9. (left) The 2-D gray level plot of the reduced distribution function of the beam $f_b^*(v_x, v_y)$. (right) Comparison of the profile of the reduced distribution function of the beam $f_b^{**}(v_x)$ (solid curve) with the profile of the drifting Maxwellian distribution function (dashed curve).

ity acquires an important component perpendicular to the magnetic field, the dispersion relation is strongly modified, and there are now three branches of solution. This is illustrated in Figure 5 for a strictly gyrating ($v_{b||} = 0$) beam with $v_{b\perp} = 7.07 v_A$. The left and middle graphs display the behavior of the frequency $\omega(k, \theta_{kB})$ for the three branches (solid curves), the first one as function of k at a given angle $\theta_{kB} = 45\,\mathrm{deg}$ of propagation with respect to the magnetic field, and the second one as a function of θ_{kB} at a given $k = |\mathbf{k}| = 7\omega_{pi}/c$.

For comparison, the whistler dispersion relation in the Maxwellian plasma without the beam is shown by a dashed curve and the resonance relation $\omega = \mathbf{k} \cdot \mathbf{v}_b$ by a dot-dashed curve. It can be seen that two of the branches are basically beam modes shifted by $\sim \pm k v_{thb}$ and interacting with the whistler mode which is supported by the background plasma. The lower and the higher branch are not found to be unstable. On the other hand, the intermediate one becomes unstable for a wide region of k vectors. This is illustrated on the right in Figure 5, where we show a contour plot of the growth rate $\gamma(k, \theta_{kB})$; the maximum growth rate $\gamma \simeq 2.5\Omega_i$ is reached for $k \simeq 6.5\omega_{pi}/c$ and $\theta_{kB} \simeq 45\,\mathrm{deg}$. This instability is resonant as may be seen from the left and middle graphs. A somewhat similar behavior of the interaction between the beam and plasma mode is reported in the case of the electron beam-plasma instability [*Dum*, 1989]. The three modes are elliptically polarized in the right-handed sense; the degree of ellipticity is close to 1 as soon as the corresponding branch lies close to the Maxwellian whistler dispersion relation (this is the case of the intermediate branch in the vicinity of the maximum of instability).

It is interesting to know how the properties of the instability depend on the various parameters of the plasma: temperatures of the various components, relative beam density, and beam velocity. The temperature of the background protons has little influence on the dispersion relation as long as the beam speed is much larger than the proton thermal speed. The instability is rather insensitive to the electron temperature; on the other hand, the growth rate depends significantly on the beam parameters: temperature, velocity, and density. This is shown in Figures 6 and 7 which display results obtained for a given angle of propagation $\theta_{kB} = 45\,\mathrm{deg}$ and with $T_{b\perp} = T_{b_{||}} \equiv T_b$ and $n_b/n_e = 0.1$ and a strictly gyrating beam, $v_{b||} = 0$ and $v_{b\perp} = 7.07 v_A$. In Figure 6 the growth rate is plotted as a function of k either for $\beta_e = 0.5$ and three different values of β_b ($\beta_b \equiv 2\mu_0 k_B n_e T_b / B_0^2$) (left) or for three values of β_e and

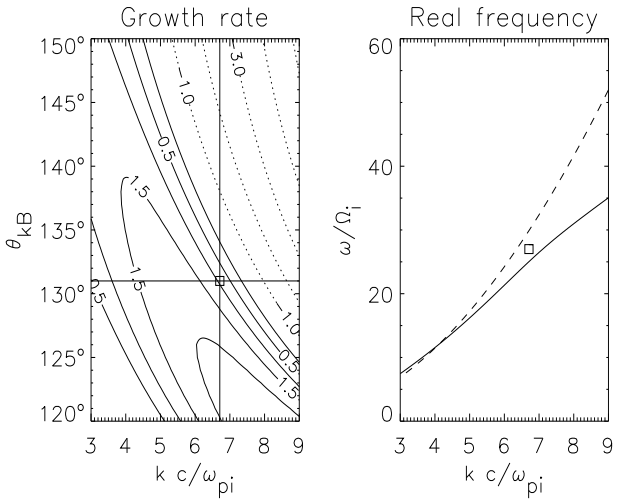

Figure 10. (left) The 2-D contour plot of the growth rate $\gamma(k, \theta_{kb})$ which results from the linear theory. (right) The dispersion relation of the real frequency $\omega(k)$ for $\theta_{kB} = 131\,\mathrm{deg}$ obtained from the linear theory for the mode in the presence of the beam (solid curve) and for the Maxwellian whistler mode (dashed curve). Small rectangle gives the parameters of the mode observed in the simulation.

$\beta_b = 0.5$ (right). Clearly, γ is almost independent of β_e, while it depends strongly on β_b.

Similarly, the dependence on the beam velocity and the beam density is illustrated in Figure 7, based on calculations using $\beta_e = \beta_b = \beta_p = 0.5$, $v_{b||} = 0$, $v_{b\perp} = v_b$. On the left the growth rate as a function of k for three different beam velocities v_b and $n_b/n_e = 0.1$ is shown, while the same function for $v_b = 7.07$ and three different values of n_b/n_e are shown on the right. Note that when changing the perpendicular velocity of the beam as on the left in Figure 7, the angle of propagation $\theta_{kB\max}$ corresponding to the maximum growth rate is shifted by a relatively small amount of about $5\,\mathrm{deg} - 10\,\mathrm{deg}$. As a result, the plotted relation $\gamma(k, \theta_{kB} = 45\,\mathrm{deg})$ is shifted in k with respect to the relation $\gamma(k, \theta_{kB} = \theta_{kB\max})$, but the maximum growth rates for the both relations are almost the same.

3.2. 1-D Hybrid Simulation of the Relaxation of the Instability

To complement the linear study just described, we have performed a 1-D, periodic, hybrid simulation for the same physical conditions. Such a numerical study will be useful for two main reasons: First, the simulations do not rely on any condition on the frequency, and therefore their results may be used to check up the prediction of the linear theory which is valid for $\omega >> \Omega_b$. Second, the simulations are self-consistent and give a correct behavior of the system during the quasi-linear stage, and we may compare the quasi-linear properties of the 1-D homogeneous simulation and the shock simulation.

The simulation box is chosen to lie along the x axis; the initial magnetic field is in the xz plane and makes an angle $\theta_{xB} = \theta_{kB} = 45\,\mathrm{deg}$ with the x axis. The spatial resolution is $dx = 0.08c/\omega_{pi}$, the number of cells is $N_x = 512$, so that the box length is $X = 40.96c/\omega_{pi}$. We have used a time step of $dt = 0.001$ (with a substepping $dt_f = dt/20$ for the advance of the magnetic field). The initial state of the plasma consists of two Maxwellian populations of protons: background protons with a density $n_p = 0.9$ and a beam with a density $n_b = 0.1$. The initial velocity of the beam $\mathbf{v}_b = 7.07 v_A$ points out of the xz plane, and the simulation was performed in the electron rest frame.

As time goes on, the bulk velocity of the beam particles rotates around the magnetic field; we shall present results obtained during a period when this velocity was in the vicinity of the xz plane. The growth rates of the modes excited in the simulation have been determined by a nonlinear fit of the time evolution of the Fourier amplitudes with damped sinusoids. Only values obtained when the correlation coefficient was greater than 0.75 are displayed. The results are shown in Figure 8, where a grey level plot denotes the (real) frequencies on the left and asterisks denote the growth rates on the right; these values were determined as described just above. Solid curves are the results of the linear theory. One can see that both real frequencies and growth rates obtained from the simulation are close to those predicted from the linear theory, except for small wave vectors for reasons which we shall discuss below.

The simulation shows clear evidence of quasi-linear effects. During its gyration toward the xz plane the beam excites a wide spectrum of k modes. These waves decelerate the resonant beam protons. This phenomenon can be seen in Figure 9. The gray level plot of the reduced (integrated over v_z) distribution function for the beam $f_b^*(v_x, v_y)$ is shown on the left; the profile of the reduced (integrated over v_y and v_z) distribution function for the beam f_b^{**} as a function of v_x (solid curve) is shown on the right. For comparison, we plot a corresponding Maxwellian distribution function (dashed curve). The beam distribution function is clearly not Maxwellian. A fraction of the resonant particles have been slowed down, and the region in velocity space where the slope of the distribution function is positive has become wider for lower velocities, and therefore lower k vector modes are exited since $\mathbf{k} \cdot \mathbf{v} \sim \omega \sim k^2$ for whistler waves. This phenomenon explains the presence of unstable modes of low k vectors which are not predicted by the linear theory (see Figure 8).

3.3. Comparison With the 3-D Simulation

In Figure 10 we compare the 3-D simulation results with those of the (homogeneous) linear theory. The contour plot of the growth rate (negative values are dotted) as a function of the magnitude k of the wave vector and of the angle θ_{kB} between this wave vector and the magnetic field is shown on the left. These growth rates result from the linear theory for values which are close to the observed ones in the shock simulation namely, the beam velocity $v_b = 4.7$, the beam density $dn_b/dn_e = 0.1$, background proton beta $\beta_p = 0.5$, the beam temperatures $T_{b||} = T_{b\perp} = T_p$ (where T_p is the temperature of background Maxwellian protons), the angle between the magnetic field, and the beam velocity $\theta_{vB} = 96\,\mathrm{deg}$. The code does not include the electron kinetics, so we set $\beta_e \simeq 0$.

The real frequency $\omega = \omega(k)$ as a function of k using dispersion relations calculated in the plasma upstream of the shock is shown on the right. The solid curve displays the dispersion relation in the presence of the beam, the dashed curve displays the dispersion relation in the Maxwellian plasma. The small rectangle gives the parameters of the mode observed in the simulation. Figure 10 shows a very good agreement of the simulation results and the linear theory. The mode observed in the simulation falls within the unstable domain as estimated from the linear theory. The fact that it does not correspond to the maximum growth rate may be simply explained by the fact that the dimensions of the simulation domain (which are

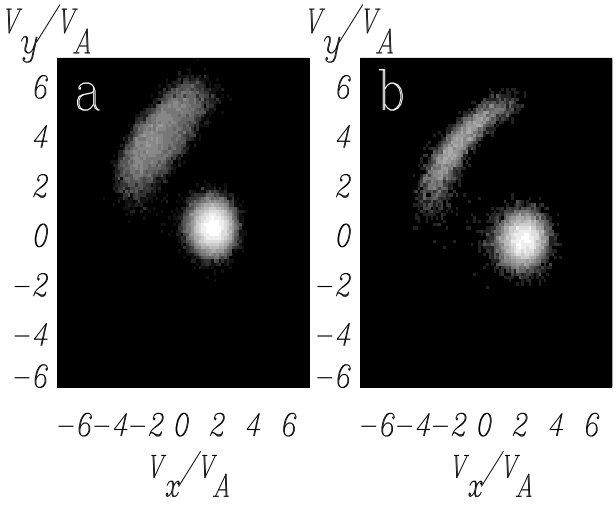

Figure 11. The 2-D gray level plots of the reduced distribution function $f(v_x, v_y)$ in the shock foot: (a) the distribution function when the whistler mode is present and (b) the distribution function when the whistler mode is not present because of a coarser resolution.

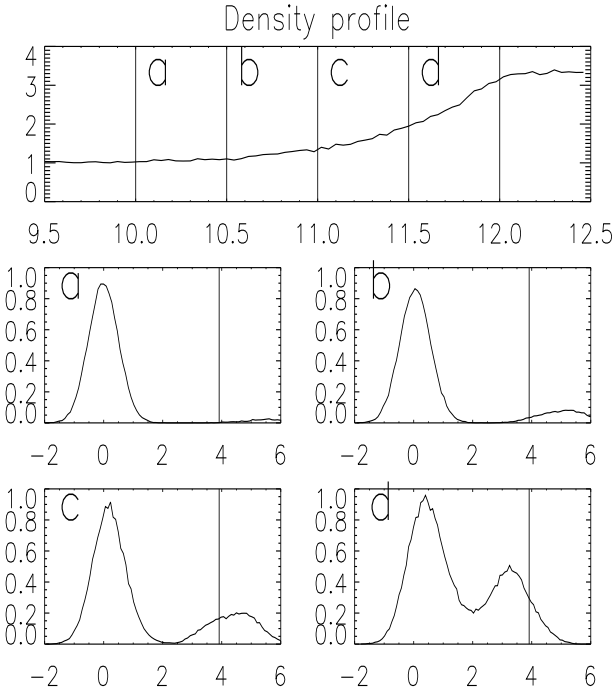

Figure 12. (top) The density profile of the shock as a reference for Figures 12a–12d. Figures 12a–12d display the profile of the reduced distribution function $f(v_k)$ of protons at different intervals indicated on the density profile. The resonance condition $v_k = \omega/k$ is denoted by a vertical line. Velocities are given in units of v_A; f is given in arbitrary units.

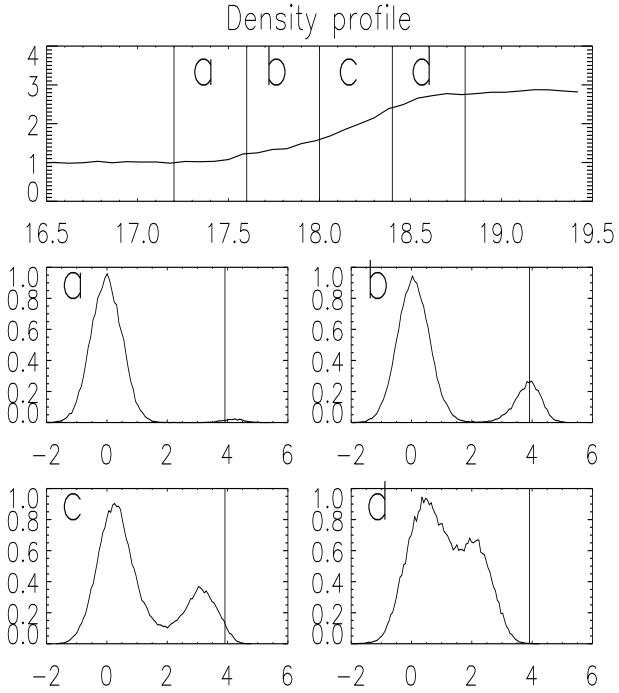

Figure 13. (top) The density profile of the shock (where some reflected protons have been removed) as a reference for Figures 13a–13d. Figures 13a–13d display the profile of the reduced distribution function $f(v_k)$ of protons at different intervals indicated on the density profile. The resonance condition $v_k = \omega/k$ is denoted by a vertical line. Velocities are given in units of v_A; f is given in arbitrary units.

quite small in the y direction) and the finite spatial resolution do not allow the excitation of the mode which is predicted to be the most unstable one by the linear theory. An influence of the inhomogeneity of the beam distribution function and a magnetic field cannot be excluded. Nevertheless, the agreement with the linear theory is reasonably good.

To illustrate the interaction of the particles with the whistler waves, we compare the results of the present simulation with those of another simulation using the same parameters but with a coarser spatial resolution ($dx = 0.25c/\omega_{pi}$ and $dy = dz = 0.5c/\omega_{pi}$). The results of both the simulations at the same time $t = 10\Omega^{-1}$ are shown in Figure 11 in the form of gray level plots of the proton velocity distribution function measured in the shock foot. The distribution obtained in the resolved simulation is displayed in Figure 11a and that obtained in the unresolved simulation is displayed in Figure 11b. In the latter case, the coarse resolution does not permit the whistlers to appear; thus Figure 11b can be considered as a reference distribution function in the absence of wave particle interactions. Therefore we can see by comparing Figures 11a and 11b that the particles are decelerated and diffused in the velocity space in much the same way as we observed in the homogeneous 1-D hybrid simulation (see section on 1-D hybrid simulation of the relaxation of the instability and Figure 9).

4. Region of Generation

If we accept that the mode is generated by a resonant beam like instability by reflected protons and that the growth rate is larger than the gyration frequency, we may find out the region of generation by looking at the location where the distribution function has a positive slope in the resonant part of velocity space. Figure 12 shows a density profile of the shock to serve as a reference for the shock profile and 1-D velocity distribution functions $f(v_k)$ in different locations with respect to the shock ramp. The velocity v_k is the projection of the velocity on the wave vector $v_k = \mathbf{v} \cdot \mathbf{k}/k$, and the distribution function $f(v_k)$ is obtained by integrating the full velocity distribution function $F(v_k, \mathbf{v}_\perp)$ over the 2-D velocity space of $\mathbf{v}_\perp$ perpendicular to $\mathbf{k}$, $f(v_k) = \int F(v_k, \mathbf{v}_\perp) \mathrm{d}^2\mathbf{v}_\perp$. The full distribution function was obtained by doing the standard statistics on the particles contained in the slices of the computational domain indicated by the intervals shown on the density profile.

The resonance condition $\mathbf{k} \cdot \mathbf{v} = kv_k = \omega$ is denoted by a vertical line. One may see that within the intervals a and b (i.e., in the foot of the shock) the resonant condition falls into the region of positive slope, whereas farther in the shock front (intervals c and d) this is not the case. This suggests that the whistler mode is generated within the foot region (with thickness about $1c/\omega_{pi}$).

This argument is strengthened by the results of the numerical experiment already mentioned in paper 1, and which consists in removing from the simulation all reflected particles upstream of some moving (escaping) boundary. When the escaping boundary lies close to the shock ramp, the generation of the whistler is inhibited, while the whistlers reappeared when this boundary was far enough from the shock ramp. The reason for the disappearance of the waves may be clearly seen in Figure 13 (same format as Figure 12), which is representative of a time when the escaping boundary is close to the shock ramp. The resonance condition in this case never falls into the interval of positive slope of the reduced distribution function (except the interval a where the density of the reflected protons is very low) and explains the absence of the whistler wave mode.

5. Dimensionality Effects

Krauss-Varban et al. [1995] have used a 2-D full-particle code with a relatively large ratio of proton to electron mass to simulate a shock with $\theta_{nB} = 60\,\mathrm{deg}$ and $M_A = 5$. They chose the simulation plane to be the coplanarity one and found upstream whistler waves similar to those observed in our simulations.

It is thus interesting to try and answer the following question: what would happen if we restricted our simulation box to two dimensions, namely, to the coplanarity plane, as in their simulation. In this case the whistler mode still exists (with a lower amplitude) but now is of course forced to remain within the coplanarity plane.

We may conclude that the velocity distribution function in the foot is unstable for waves propagating within a wide range of angles with respect to the coplanarity plane because of the complicated velocity distribution function in the foot (see Figuri 11). A well-resolved, large-scale 3-D code is required if one wants to keep the most unstable modes. We expect that the most unstable modes in the case of *Krauss-Varban et al.* [1995] are out of the coplanarity plane and therefore out of the simulation plane, but the angle between the most unstable modes and the coplanarity plane can be small (as we shall discuss in next session).

This comparison suggests also that the electron dynamics, taken into account by *Krauss-Varban et al.* [1995], does not generally damp out the instability. This is in agreement with the results of the linear theory, which show that the instability is not sensitive to the electron temperature (see section on the properties of the instability for a gyrating beam and Figure 6), and it may also be regarded as a justification of the use of the hybrid code which allowed us to go to three dimensions (although a larger computational domain would be welcome).

6. Comparison With Observations

6.1. Simulation

The whistler mode found in the simulation possesses many properties of the observed upstream whistlers: frequencies within the range $20 - 40\Omega_i$, and right-handed polarization. They propagate upstream from the shock obliquely to the magnetic field at angles from $10\,\mathrm{deg}$ to $50\,\mathrm{deg}$ [*Fairfield*, 1974; *Orlowski and Russell*, 1991].

However, the wave vector of the simulation whistlers makes a finite angle, $\theta_{kc} \simeq 56\,\mathrm{deg}$, with the coplanarity plane and with the shock normal, $\theta_{kn} \simeq 51\,\mathrm{deg}$, although *Orlowski et al.* [1994], in a recent study of upstream whistlers at the Venus bowshock found that the observed wave vectors are distributed mostly in the coplanarity plane and usually within a small angle from the shock normal.

A first explanation is that, as explained above, because of the limitations in the size of our computational domain, we did not allow for the most unstable mode; however, even in the linear theory this most unstable mode is propagating fairly obliquely with respect to either the coplanarity plane or the shock normal. A better possible explanation is that we have considered here only a simple but rather special case not very well represented in the data; indeed, the shock is close to being perpendicular. More typical shock waves have higher Mach numbers and are more oblique. It is expected that for more oblique shocks, where the beam velocity has a significant component along the magnetic field, the most unstable wave vector will come closer to the coplanarity plane. Moreover, for the propagation against the solar wind we should require the normal component of the phase velocity to be greater then the bulk upstream velocity. For higher Mach number shocks this condition will inhibit propagation at high oblique angles to the shock normal because such waves will be convected and have little time to grow. So for more typical shocks the excited modes will have tendency to become aligned with the shock normal in agreement with the results of *Orlowski et al.* [1994]. These problems are beyond the scope of the present paper and are under investigation.

6.2. Linear Theory

The linear theory of the gyrotropic gyrating beam in Maxwellian plasma gives the results which are in good agreement with the observations. Indeed, the intermediate mode is right-handed and almost circularly polarized within the unstable region, and it reaches its maximum growth rate at oblique propagation with respect to the background magnetic field. The mode is unstable within a wide range of wave vectors which are compatible with the broadband character of upstream whistlers [*Orlowski et al.*, 1995]. The frequencies found within the unstable region are comparable to the observed ones (see, for example, Figure 5). These properties and the relative insensitivity of the instability to the electron temperature make the instability a good candidate for the generation mechanism of upstream whistlers for a wide range of plasma parameters.

7. Conclusions

In this work we have substantiated the generation mechanism of upstream whistlers near the shock proposed in paper 1 and proposed independently by *Krauss-Varban et al.* [1995]. We have discussed the evidence from numerical simulations and linear theory in favor of a scenario where the upstream whistlers are generated by the reflected protons when they gyrate back to the shock; in this region their distribution function presents a positive, unstable slope in velocity space which is unstable for the excitation of whistler waves. The removal of the reflected particles causes the disappearance of the whistler modes because they are resonant everywhere with protons which happen to belong to the stable part of the distribution function.

We have extended the comparison of the simulation results of paper 1 with linear theory in an approximation which was proposed by *Wong and Goldstein* [1988], with good agreement for the growth rates and angles of propagation. The properties of the simulation whistlers correspond to those of the upstream whistlers found in the foreshock of planetary shocks except for the direction of propagation which lies at the boundary of the domain where those whistlers are usually seen.

Finally, we have shown that slightly supercritical quasi-perpendicular shocks do not present AIC shock front rippling, because such an AIC mode has not enough time to reach a large amplitude while is transported through the shock ramp.

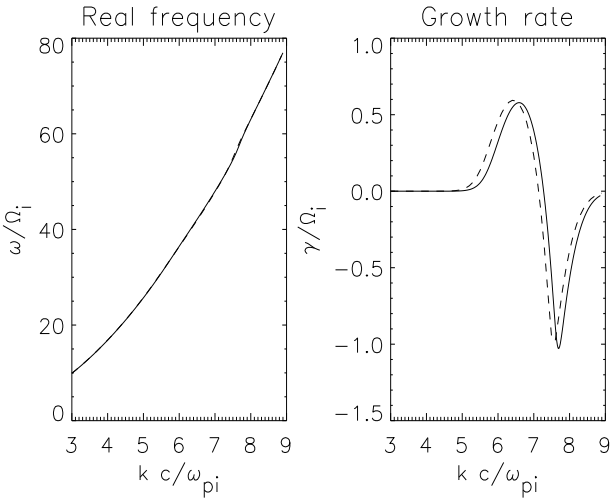

Figure 14. The comparison of the exact dispersion relation (equation A2) (dashed curve) and the approximated one (equation A1) (solid curve) for (left) the frequency $\omega(k)$ and (right) the growth rate $\gamma(k)$.

Appendix A: Appendix: Instability of a Gyrating Nonmagnetized Ion Beam

The dispersion properties of a homogeneous plasma with a Maxwellian proton and electron core and a beam of gyrating protons may be described in the high-frequency range $\omega >> \Omega_i$ by the dispersion tensor $\mathbf{D} = \mathbf{D}_e + \mathbf{D}_p + \mathbf{D}_b$, where $\mathbf{D}_e$ and $\mathbf{D}_p$ are the standard contributions of electrons and protons, respectively, with a (drifting) bi-Maxwellian distribution function:

$$f_\alpha(\mathbf{v}) = \frac{n_\alpha}{\sqrt{\pi}^3 v_{th\perp\alpha}^2 v_{th||\alpha}} \times \exp\left(-\frac{v_\perp^2}{v_{th\perp\alpha}^2} - \frac{(v_{||} - v_{0||\alpha})^2}{v_{th||\alpha}^2}\right)$$

where $\alpha \in \{e, p\}$ denotes the particle species (electron, protons). The magnetic field is parallel to the z axis, $\mathbf{B}_0 = (0, 0, B_0)$, and the wave vector is chosen to lie in the xz plane $\mathbf{k} = (k_\perp, 0, k_{||})$. The nonmagnetized gyrating ion beam is presumed to have a drifting bi-Maxwellian distribution with a velocity which lies in the xz plane $\mathbf{v}_{0b} = (v_{0\perp b}, 0, v_{0||b})$

$$f_b = \frac{n_b}{\sqrt{\pi}^3 v_{th\perp b}^2 v_{th||b}} \times \exp\left(-\frac{(v_x - v_{0\perp b})^2}{v_{th\perp b}^2} - \frac{v_y^2}{v_{th\perp b}^2} - \frac{(v_z - v_{0||b})^2}{v_{th||b}^2}\right)$$

In the high-frequency range $\omega >> \Omega_b$ we may neglect the beam gyration so that the beam contribution may be given as given by *Wong and Goldstein* [1988]. The solution $\omega(\mathbf{k})$ of the dispersion relation, given by

$$\det(\mathbf{D}) = 0 \tag{A1}$$

is found numerically using standard methods.

Note that our definition of the Alfvén velocity uses the total electron density n_e, which is at variance with the definition used by *Wong and Goldstein* [1988] which is based on n_p. The calculation is done in the frame where the parallel electron velocity is zero, $v_{0||e} = 0$, and $v_{0||p} = -n_b/n_e v_{0||b}$.

As proposed by *Wong and Goldstein* [1988], the validity of the approximation (and the correctness of the code) may be tested by the comparison with the exact dispersion relation, which is known

when the ion beam velocity is parallel to the magnetic field. For this case and restricting ourselves to the wave vectors k parallel to the ambient magnetic field, we have the following simple dispersion relation:

$$\frac{k^2c^2}{\omega^2} = 1 + \sum_\alpha \frac{\omega_{p\alpha}^2}{\omega^2}[A_\alpha - 1 + \frac{(\omega - k_{||}v_{0||\alpha} + \Omega_\alpha)A_\alpha - \Omega_\alpha}{k_{||}v_{th||\alpha}} Z(\frac{\omega - k_{||}v_{0||\alpha} + \Omega_\alpha}{k_{||}v_{th||\alpha}})] \quad \text{(A2)}$$

where $\alpha \in \{e, p, b\}$ denotes the different species, $\omega_{p\alpha}$ is the plasma frequency of the species α, A_α is the temperature anisotropy $A_\alpha = v_{th\perp\alpha}^2/v_{th||\alpha}^2$, and Z is the plasma function.

The result of the comparison for $\beta_{e||} = 0.001$ end $\beta_{p||} = 0.5$ is shown in Figure 14, which shows the frequency $\omega = \omega(k)$ (left) and the growth rate $\gamma = \gamma(k)$ (right) calculated with the approximate equation (A1) (solid curve) and with the exact one (A2) (dashed curve). The results for the unmagnetized beam are similar to the exact calculations but are shifted in k vector space, because of the presence of a term $\Omega_b/(kv_{th||b})$ in the relation (A2). The real frequencies are essentially the same in both cases. We may thus conclude that the numerical resolution of the relation (A1) gives satisfactory results at least for parallel propagation. The growth rates and frequencies are in good agreement with the exact values, but growth rates are shifted in k space as one replaces the cyclotron resonance by the Landau resonance. One may expect this difference to be less pronounced for more oblique propagation. The difference is also smaller for higher beam temperatures [see *Wong and Goldstein*, 1988, who have found a good agreement between the two dispersion relations for $\beta_{p||0} = 1$ and $T_b = T_{p||}$].

We have also compared our results with those given by *Wong and Goldstein* [1988] and found the same results when using the same parameters. This is illustrated in Figure 15. Contour plots of the growth rate for a gyrating beam $v_{0||b} = 0$, $v_{0\perp b} = 7.07/\sqrt{0.9}$ (we have a different definition of the Alfvén velocity), $\beta_e = \beta_p = 1$ are shown on the left. The dispersion relation $\omega = \omega(\theta_{kB})$ (solid curve) and $\gamma = \gamma(\theta_{kB})$ (dashed curve) for $k = 5.6/\sqrt{0.9}\omega_{pi}/c$ (in logarithmic scale) are shown on the right. The results are the same as given by *Wong and Goldstein* [1988, Figure 4].

Acknowledgments.

This work was supported in part by the US-Czech Science and Technology Joint Fund under project 95043 and by Grant Agencies of the Czech Republic (205/96/1575) and of the Academy of Science of the Czech Republic (A3042601).

The Editor thanks D. Krauss-Varban and another referee for their assistance in evaluation this paper.

References

Burgess, D., Simulations of backstreaming ion beams formed at oblique shocks by direct reflection, *Ann. Geophys.*, *5A*, 133–146, 1987.

Dum, C. T., Transition in the dispersive properties of beam-plasma and two-stream instabilities, *J. Geophys. Res.*, *94*, 2429–2442, 1989.

Fairfield, D. H., Whistler waves observed upstream from collisionless shocks, *J. Geophys. Res.*, *79*, 1368–1378, 1974.

Feldman, W. C., R. C. Anderson, S. J. Bame, S. P. Gary, J. T. Gosling, D. J. McComas, M. F. Thomson, G. Paschmann, and M. M. Hoppe, Electron velocity distribution near the Earth's bow shock, *J. Geophys. Res.*, *88*, 96–110, 1983.

Gary, S. P., S. A. Fuselier, and B. J. Anderson, Ion anisotropy instabilities in the magnetosheath, *J. Geophys. Res.*, *98*, 1481–1488, 1993.

Gedalin, M., Ion reflection at the shock front revisited, *J. Geophys. Res.*, *101*, 4871–4878, 1996.

Greenstadt, E. W., R. W. Fredricks, C. T. Russell, F. L. Scarf, R. R. Anderson, and D. A. Gurnett, Whistler mode wave propagation in the solar wind near the bow shock, *J. Geophys. Res.*, *86*, 4511–4516, 1981.

Hellinger, P., A. Mangeney, and A. Matthews, Whistler waves in 3D simulations of quasi-perpendicular shocks, *Geophys. Res. Lett.*, *23*, 621–624, 1996.

Hoppe, M. M., C. T. Russell, T. E. Eastman, and L. A. Frank, Characteristics of the ULF waves associated with upstream ion beams, *J. Geophys. Res.*, *87*, 643–650, 1982.

Krauss-Varban, D., F. G. Pantellini, and D. Burgess, Electron dynamics and whistler waves at quasi-perpendicular shocks, *Geophys. Res. Lett.*, *26*, 2091–2094, 1995.

Matthews, A., Current advance method and cyclic leapfrog for 2D multispecies hybrid plasma simulations, *J. Comput. Phys.*, *112*, 102–116, 1994.

McKean, M. E., N. Omidi, and D. Krauss-Varban, Wave and ion evolution downstream of quasi-perpendicular bow shocks, *J. Geophys. Res.*, *100*, 3427–3431, 1995.

McKean, M. E., N. Omidi, and D. Krauss-Varban, Magnetosheath dynamics downstream of low Mach number shocks, *J. Geophys. Res.*, *101*, 20,013–20,022, 1996.

Orlowski, D. S., and C. T. Russell, Ulf waves upstream of the Venus bow shock: Properties of one-Hertz waves, *J. Geophys. Res.*, *96*, 11,271–11,282, 1991.

Orlowski, D. S., G. K. Crawford, and C. T. Russell, Upstream waves at Mercury, Venus and Earth: Comparison of properties of one-Hertz waves, *Geophys. Res. Lett.*, *17*, 2293–2296, 1990.

Orlowski, D. S., C. T. Russell, and R. Lepping, Wave phenomena in the upstream region of Saturn, *J. Geophys. Res.*, *97*, 19,187–19,199, 1992.

Orlowski, D. S., C. T. Russell, D. Kraus-Varban, and N. Omidi, On the source of upstream whistlers in the venus foreshock, in *COSPAR Colloquia, Plasma environments of non-magnetic Planets*, vol. 4, edited by T. I. Gombosi, pp. 217–227, Pergamon Press, New York, 1994.

Orlowski, D. S., C. T. Russell, D. Krauss-Varban, N. Omidi, and M. F. Thomsen, Damping and spectral formation of upstream whistlers, *J. Geophys. Res.*, *100*, 17,117–17,128, 1995.

Rodriguez, P., and D. A. Gurnett, Electrostatic and electromagnetic turbulence associated with the Earth's foreshock, *J. Geophys. Res.*, *80*, 19–27, 1975.

Rönmark, K., WHAMP-waves in homogeneous, anisotropic, multicomponent plasmas, *Tech. Rep. 179*, Kiruna Geophysical Institute, 1982.

Russell, C. T., D. D. Childers, and P. J. Coleman, OGO 5 observation of upstream waves in the interplanetary medium, *J. Geophys. Res.*, *76*, 845–862, 1971.

Sentman, D. D., M. F. Thomsen, S. P. Gary, W. Feldman, and M. M. Hoppe, The oblique whistler instability in the Earth's foreshock, *J. Geophys. Res.*, *88*, 2048–2056, 1983.

Skopke, N., G. Paschmann, S. J. Bame, J. T. Gosling, and C. T. Russell, Evolution of ion distribution across the nearly perpendicular bow shock: Specularly and nonspecularly reflected gyration ions, *J. Geophys. Res.*, *88*, 6121–6136, 1983.

Thomas, V. A., and S. H. Brecht, Two-dimensional simulation of high Mach number plasma interactions, *Phys. Fluids*, *29*, 2444–2454, 1986.

Tokar, R. L., and D. A. Gurnett, The propagation and growth of whistler mode waves generated by electron beams in the Earth's bow shock, *J. Geophys. Res.*, *90*, 105–114, 1985.

Veltri, P., and G. Zimbardo, Electron-whistler interactions at the Earth's bow shock, 1, Whistler instability, *J. Geophys. Res.*, *98*, 13,325–13,333, 1993.

Winske, D., and K. B. Quest, Magnetic field and density fluctuations at perpendicular supercritical shocks, *J. Geophys. Res.*, *93*, 9681–9693, 1988.

Wong, H. K., and M. L. Goldstein, Proton beam generation of whistler waves in the Earth's foreshock, *J. Geophys. Res.*, *92*, 12,419–12,424, 1987.

Wong, H. K., and M. L. Goldstein, Proton beam generation of oblique whistler waves, *J. Geophys. Res.*, *93*, 4110–4114, 1988.

P. Hellinger, Institute of Atmospheric Physics, Prague 14131, Czech Republic. (e-mail: petr.hellinger@ufa.cas.cz)

A. Mangeney, Observatory of Paris, Meudon 92190, France. (e-mail: mangeney@megasg.obspm.fr)

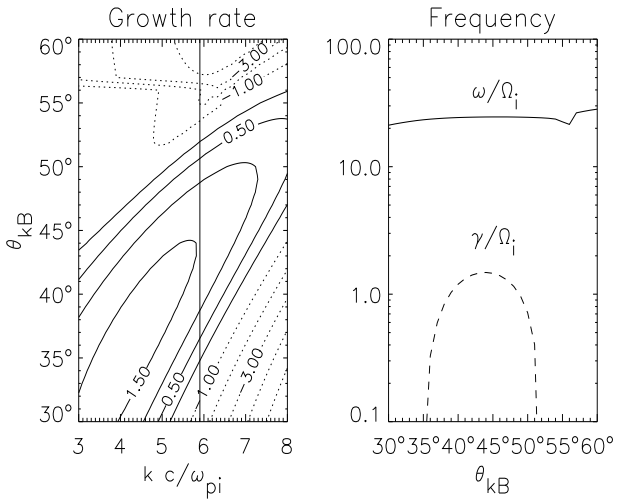

Figure 15. (left) The 2D contour plot of the growth rate $\gamma(k, \theta_{kB})$ (negative values of γ are dotted). (right) The profiles of the frequency $\omega(\theta_{kB})$ (solid curve) and the growth rate $\gamma(\theta_{kB})$ (dashed curve) for $k = 5.6/\sqrt{0.9}\omega_{pi}/c$ (in logarithmic scale). The same values as given by *Wong and Goldstein* [1988, figure 4] are used.